JOURNAL OF MORPHOLOGY 276:1146–1156 (2015)

Morphology, Microstructure, Crystallography, and Chemistry of Distinct $CaCO_3$ Deposits Formed by Early Recruits of the Scleractinian Coral *Pocillopora damicornis*

Melany Gilis,[1,2] Anders Meibom,[1,2]* Duncan Alexander,[3] Olivier Grauby,[4] Jarosław Stolarski,[5] and Alain Baronnet[4]

[1]*Laboratory for Biological Geochemistry, School of Architecture, Civil and Environmental Engineering (ENAC), Ecole Polytechnique Fédérale de Lausanne (EPFL), Lausanne CH-1009, Switzerland*
[2]*Center for Advanced Surface Analysis, Institute of Earth Sciences, University of Lausanne, Lausanne CH-1009, Switzerland*
[3]*Interdisciplinary Centre for Electron Microscopy, Ecole Polytechnique Fédérale de Lausanne, Switzerland*
[4]*Aix-Marseille Université and Centre Interdisciplinaire de Nanosciences De Marseille (CINaM), Campus de Luminy, Marseille 13288, France*
[5]*Institute of Paleobiology, Polish Academy of Sciences, Twarda 51/55, Warsaw PL-00-818, Poland*

ABSTRACT Scleractinian corals begin their biomineralization process shortly after larval settlement with the formation of calcium carbonate ($CaCO_3$) structures at the interface between the larval tissues and the substrate. The newly settled larvae exert variable degrees of control over this skeleton formation, providing an opportunity to study a range of biocarbonate structures, some of which are transient and not observed in adult coral skeletons. Here we present a morphological, structural, crystallographic, and chemical comparison between two types of aragonite deposits observed during the skeletal development of 2-days old recruits of *Pocillopora damicornis*: (1) Primary septum and (2) Abundant, dumbbell-like structures, quasi-randomly distributed between initial deposits of the basal plate and not present in adult corals—At the mesoscale level, initial septa structures are formed by superimposed fan-shaped fasciculi consisting of bundles of fibers, as also observed in adult corals. This organization is not observed in the dumbbell-like structures. However, at the ultrastructural level there is great similarity between septa and dumbbell components. Both are composed of <100 nm granular units arranged into larger single-crystal domains.Chemically, a small difference is observed between the septae with an average Mg/Ca ratio around 11 mmol/mol and the dumbbell-like structures with ca. 7 mmol/mol; Sr/Ca ratios are similar in the two structures at around 8 mmol/mol—Overall, the observed differences in distribution, morphology, and chemistry between septa, which are highly conserved structures fundamental to the architecture of the skeleton, and the transient, dumbbell-like structures, suggest that the latter might be formed through less controlled biomineralization processes. Our observations emphasize the inherent difficulties involved in distinguishing different biomineralization pathways based on ultrastructural and crystallographical observations. J. Morphol. 276:1146–1156, 2015.

KEY WORDS: biocalcification; aragonite; coral recruits; dumbbell; septa; TEM

INTRODUCTION

Proposed biomineralization mechanisms in adult scleractinian corals range from biologically induced, that is, precipitation regulated primarily by physico-chemical and environmental parameters (Bryan and Hill, 1941; Barnes, 1970; Weber, 1973; Constantz, 1986; Veis, 2005; Ries et al., 2006; Holcomb et al., 2009), over combinations of both abiotic and biotic processes (Vandermeulen and Watabe, 1973; Gladfelter, 1982, 1983; Lowenstam and Weiner, 1989; Cohen et al., 2009; Juillet-Leclerc et al., 2009; Goffredo et al., 2011; Venn et al., 2013; Robinson et al., 2014), to strict biological control highly regulated with an organic matrix component (e.g., Jell, 1974; Johnston, 1978, 1980; Le Tissier, 1988a, 1991; Clode and Marshall, 2002a,b; Cuif and Dauphin, 2005a,b; Tambutté

Additional Supporting Information may be found in the online version of this article.

Contract grant sponsor: European Research Council; Grant number: 246749 (BIOCARB); Contract grant sponsor: Ecole Polytechnique Féderale de Lausanne (to A.M.).

*Correspondence to: Anders Meibom; Laboratory for Biological Geochemistry Ecole Polytechnique Fédérale de Lausanne (EPFL) School of Architecture, Civil and Environmental Engineering GR C2 524, Station 2 – CH-1015 Lausanne.
E-mail: anders.meibom@epfl.ch

Received 13 November 2014; Revised 11 February 2015; Accepted 28 April 2015.

Published online 21 July 2015 in Wiley Online Library (wileyonlinelibrary.com).
DOI 10.1002/jmor.20401

et al., 2007; Meibom et al., 2004, 2006, 2008; Houlbrèque et al., 2009; Brahmi et al., 2012a,b).

This debate, which is not restricted to coral biomineralization (Cuif et al., 2011), is partly the result of difficulties in defining clear criteria (morphological, structural, crystallographic, and chemical) for distinguishing biomineralization pathways. In general, biologically induced biominerals are considered more likely to have crystal-chemical features akin to minerals formed abiotically under similar environmental conditions, while biologically controlled mineralization should give rise to functional and species-specific structures with mineralogical features that are different from their inorganic counterparts and irreproducible in biomimetic *in vitro* synthesis (Mann, 2001). However, recent work, for example, with carbonate precipitation in gel-environments, have brought to light new pathways for inorganically producing materials with features resembling biominerals (Asenath-Smith et al., 2012; Sánchez-Navas et al., 2013), further complicating the distinction between biologically controlled/induced and purely abiotic mineral formation. Interestingly, the onset of carbonate mineralization at the interface between a newly settled coral larva and its substrate provides an opportunity to study processes with various levels of biological control taking place simultaneously.

Only few studies have investigated biomineralization in recently settled scleractinian coral larvae (Wainwright, 1963; Vandermeulen and Watabe, 1973; Johnston, 1976; Goreau and Hayes, 1977; Jell, 1980; Le Tissier, 1988a; Cohen et al., 2009; Clode et al., 2011). Recently, Gilis et al. (2014) carried out a multiscale, microscopic, and spectroscopic investigation of all skeletal elements deposited by *Pocillopora damicornis* recruits, from 12 hours to 22 days after settlement in aquarium conditions on a flat substrate. From a macro-structural point of view, the sequence of calcium carbonate deposition defined in this study was consistent with previous descriptions of biomineralization by *Pocillopora damicornis* recruits (Vandermeulen and Watabe, 1973; Le Tissier, 1988a). Aragonite was the major phase, with the exception of tiny rod-shaped crystals with a calcitic component, present only in the very first stages of basal plate formation (Gilis et al., 2014). At the micrometer-scale, a wide range of complex morphologies from aragonitic dumbbell-like and semispherulitic structures was uncovered, randomly distributed on the substrate in areas where the basal plate was not yet completed. These observations highlight the mineralogical and morphological diversity in the early stages of larval biomineralization and strongly suggest that several different mechanisms are at play.

Here, we use transmission and scanning electron microscopy (TEM and SEM), electron diffraction, and energy-dispersive X-ray spectroscopy to compare morphological, (internal-) structural, crystallographic, and compositional features of dumbbell-like structures and of primary septa, which form simultaneously during skeleton development by 2-days old recruits of *Pocillopora damicornis*.

MATERIAL AND METHODS

Larval Collection and Settling

Colonies (about 15 cm in diameter) of the symbiotic reef-building coral species *Pocillopora damicornis* (Linnaeus, 1758) were grown in 700 l aerated, closed-circuit artificial SW aquarium (Aquarium Tropical, Palais de la Porte Dorée, Paris, France) under the following conditions: 25 ± 2°C, 12 h/12 h light/dark cycle; 4000 Lux; 100 micromol photons m^{-2} s^{-1} (PAR); pH = 8.1; Salinity = 35%. Planula larvae released from a large colony were transferred into Lumox® Petri dishes for settlement and sampled at different stages of growth (about 24, 36, 48, 72, and 96 hours after settlement; c.f. Gilis et al., 2014 for further details). *In vivo* pictures of recruits were taken of three or more larvae at different stages of their development with a digital camera fitted on a stereomicroscope (SM) or on a bright-field inverted microscope (BIM).

Sample Preparation and Observation

Petri dishes containing recruits in Stage C (Gilis et al., 2014), that is, about 48 hours after settlement, were bleached in 1% sodium hypochlorite until all tissue was removed (2×1 h) then rinsed with 0.22 μm-filtered tap-water (pH = 7.3; 20 min) and stored in absolute ethanol until further treatment for microscopic observation. Prior tests of different dilutions of hypochlorite and H_2O_2 solutions were conducted on biogenic and abiogenic aragonite and calcite samples in order to select the optimal bleaching solution. These tests confirmed that sodium hypochlorite is the optimal agent for dissolving epithelial tissue and expose coral skeleton for microstructural investigations, in agreement with previous work with the coral *Galaxea fascicularis* (Clode and Marshall, 2003). Note that filtered tap water was deliberately used for rinsing instead of deionized or distilled H_2O, which can induce skeletal dissolution due to its low ionic strength. All solutions were gently added to and removed from the dishes in order to minimize solution motion around skeletal deposits, which may cause displacements. Twelve hours before microscopic analysis, dishes preserved in absolute ethanol were oven-dried at 38°C. Drying the samples stored in ethanol instead of water avoids recrystallization on the skeletal surface. Individual, naked skeletons formed on the 25 μm thick Lumox® film were carefully mounted on aluminum stubs and carbon-coated for ultrastructural study.

Low resolution micrographs of remaining skeleton mounted on aluminum stubs were acquired with a digital camera fitted on a stereomicroscope (SM) prior to their observation with the scanning electron microscope (SEM) JEOL JSM-6320F at CINaM (Aix-Marseille Université), working at 15 kV.

Focused ion beam (FIB) ultrathin sections were extracted from a primary septum and from a dumbbell-like structure, transversal and parallel to their longitudinal plane, using a dual beam SEM/FIB FEI Helios NanoLab 600 (CP2M, Marseille) or a ZeissNVision 40 CrossBeam (EPFL, Lausanne). To avoid any folding during the milling, we restricted the size of the FIB lamellas to 5–7 μm in width and 8–10 μm in height. The FIB sectioning consisted of the following steps: (i): a protective platinum or carbon layer of about 1.5 μm thickness was deposited upon the surface in the region of interest; (ii): trenches were then milled at 30 kV on both sides of this layer to create a 300–500 nm thick foil (reducing current from 6 nA to 80 pA while thinning); (iii): using a micromanipulator, *in situ* lift-out was performed by sputtering a platinum layer to connect the micromanipulator tip with the TEM foil; (iv): the TEM

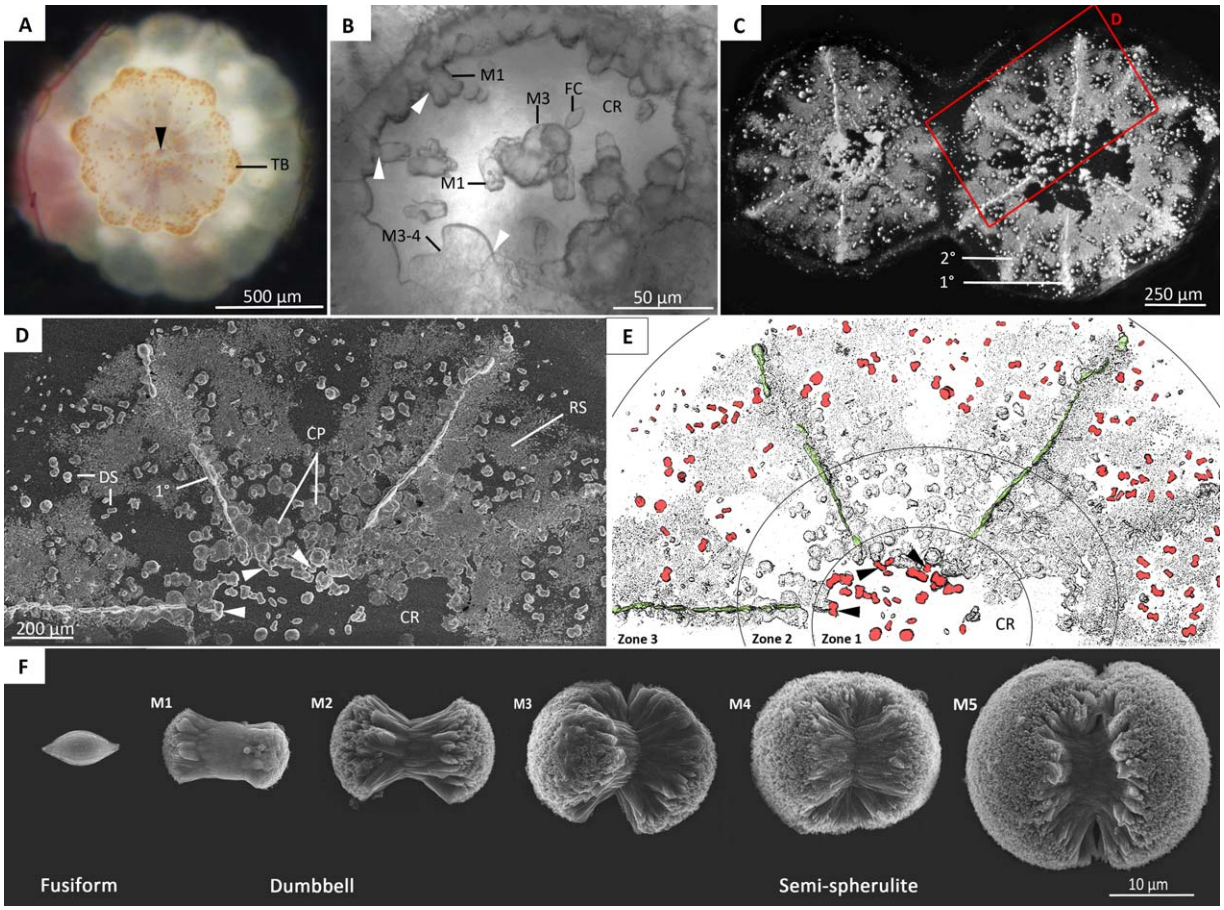

Fig. 1. *Pocillopora damicornis* $CaCO_3$ deposits in Stage C. (**A**) *In vivo* picture of Stage C recruit (SM). (**B**) $CaCO_3$ deposits observed *in vivo* in the central zone 1 (BIM). (**C**) $CaCO_3$ deposits on the Lumox substrate observed after bleaching of tissues (SM). (**D**) SEM magnification of the forming basal plate shown in (C). (E) (D) after image processing enhancing the spatial distribution of fusiform, dumbbell-like, and semispherulitic structures (in red) and primary septa (1°, in green). (F) Different morphs of fusiform-like, dumbbell-like and semispherulitic structures. TB: tentacle buds, CR: future columella region (zone 1), DS: dumbbell-like structure, FC: fusiform crystal, CP: circular platelets, RS: rod-shaped crystals., M1–M5: morphs 1–5 of dumbbell-like structures, 1°: primary septum, 2°: secondary septum; Arrowheads point to individual dumbbell-like objects. [Color figure can be viewed in the online issue, which is available at wileyonlinelibrary.com.]

foil was attached to a Cu TEM grid and a final FIB thinning and cleaning at 5 kV/40 pA were carried out to obtain a foil of less than 100 nm thick.

Thinned lamella were then observed on a transmission electron microscope (TEM) JEOL 3010 at 300 kV (primary septum, CINaM, Marseille) and JEOL 2200FS at 200 kV (dumbbell-like structure, CIME-EPFL, Lausanne) for bright-field and dark-field imaging and recording selected area electron diffraction (SAED) patterns. We used low dose illumination during tuning of the objective focus and astigmatism correction to reduce potential damages to the samples. SAED diagrams were obtained by using a set of selection apertures, thus selecting skeletal regions of interest including one to several biomineral fibers at a time. When working on the FIB section of the septum no tilt was applied. This allowed easy correlation between crystallographic orientations and the morphology of the septum. Indexations of SAED patterns were done manually by matching the observed patterns with those of standard aragonite, simulated under kinematic diffraction conditions using the SingleCrystal software coupled with the CrystalMaker application. Dark-field images were obtained from a selected single, low angle, and bright-diffracted beam without alignment correction of the gun. Owing to fiber-texture (see below), a single diffraction spot corresponds to one, or occasionally more, superimposed reflections.

Energy-dispersive X-ray spectroscopy (EDX) analysis was achieved on both FIB sections with a FEI Tecnai Osiris (80 KV; 0.047 nA). The four windowless Super-X SDD EDX detectors integrated into the pole piece allowed high speed and high sensitivity EDX elemental measurements in scanning transmission electron microscopy (STEM) mode without altering the biomaterial. Lack of significant beam damage was testified by total absence of CaO powder diffraction rings on the Ca-carbonate SAED pattern.

To compare Mg/Ca and Sr/Ca ratio (mmol/mol) in septa and dumbbell-like structures, we acquired six STEM hypermaps data per FIB section from which individual spectra were extracted and processed for semiquantitative analysis (Cliff-Lorimer technique; 2 sigma) with the software Esprit 1.9. Unspecific peaks were deconvoluted except for Ca, Mg, and Sr and background correction was applied manually. Mg/Ca and Sr/Ca ratio were obtained assuming a homogenous section thickness of 100 nm and a density of 2.95 g/cm^3. Realistic variations in thickness of FIB sections might account for 10–15% variations in the resulting Mg/Ca and Sr/Ca ratios.

Finally, growing septa (distinguished from the basal plate), were gently crushed in a mortar with pestle. Resulting micron- or submicron-scale fragments were placed on holey carbon-coated copper grids. Air-dried preparations were then observed on a JEOL 3010 TEM at 300 kV for TEM imaging and for

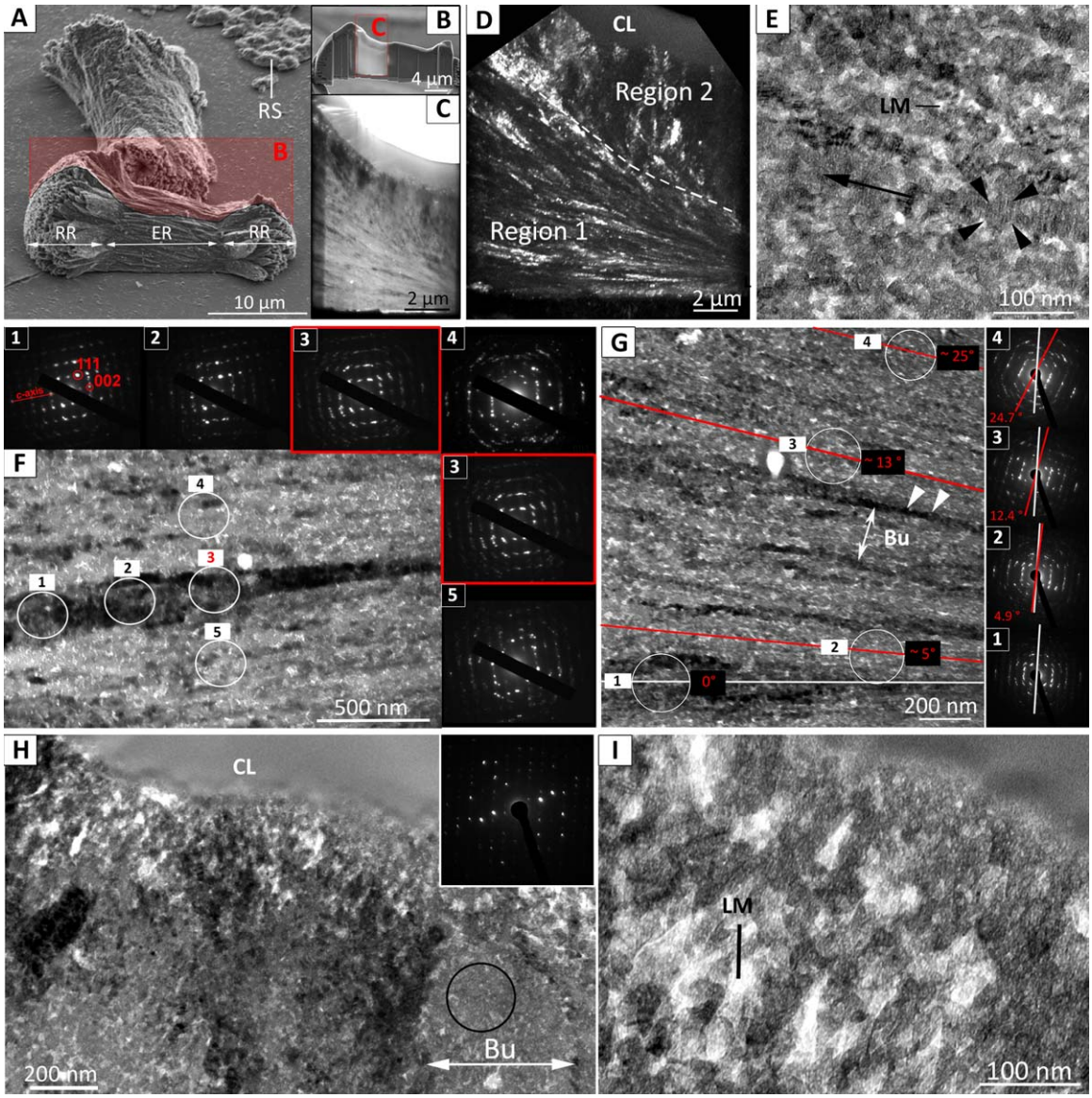

Fig. 2. *Pocillopora damicornis* dumbbell-like structures in a Stage C recruit. (**A**) Two dumbbell-like structures on the substrate (SEM). (**B**) FIB lamella lifted out from the dumbbell-like structure in (A) (SEM). (**C**) Bright-field micrograph of the thinned area in the FIB lamella (BF-TEM). (**D**) Dark-field micrograph in the thinned area of the FIB lamella exhibiting different regions (DF-TEM). (**E**) Stack of granular fibers separated by beam-sensitive lighter material (BF-TEM). (**F**) Bundles of granular fibers in region 1 (BF-TEM) with SAED patterns recorded along a small bundle of fibers displaying a strongest diffraction contrast (1–3) and in two adjacent bundles (4-5). (**G**) SAED patterns across strongly diverging bundles of fibers with a rotation of the *c*-axis following faithfully the rotation of the fibers and their elongation (1–4) (BF-TEM). (**H**) Granular bundles in region 2 without defined fibrillar organization (BF-TEM) that appear like large clusters of coherently oriented 20–50 nm grains (inset: SAED pattern from black circle selection). (I) Lighter and beam-sensitive material in region 2 (BF-TEM). Bu: bundle; CL: carbon layer; ER: elongated region; LM: light material; RR: radiating region; RS: rod-shaped structures. Black arrowheads: encircling granular unit. White arrowheads: individual fiber. Black arrow: elongation of a fiber. [Color figure can be viewed in the online issue, which is available at wileyonlinelibrary.com.]

SAED patterns recording in addition to observations made on sections prepared by FIB milling.

RESULTS

Distribution of $CaCO_3$ Deposits by 2-Days Old Coral Recruits

Settled, 2-days old recruits of *Pocillopora damicornis* have developed tentacle buds (Fig. 1A) and an initial skeleton with an almost continuous basal plate, consisting of fused rod-shaped crystals (RS, zone 2-3, Fig. 1D,E), circular platelets (CP, zone 2, Fig. 1D,E), 10–20 µm high primary septa, and nascent secondary septa (Fig. 1C–E). Dumbbell-like to semispherulitic structures are randomly distributed in zone 1 (Fig. 1B,D,E), sometimes fused with the surrounding circular flat structures (Fig. 1B,D) and also present in interseptal areas of zone 3 (Fig. 1D,E). Very rare

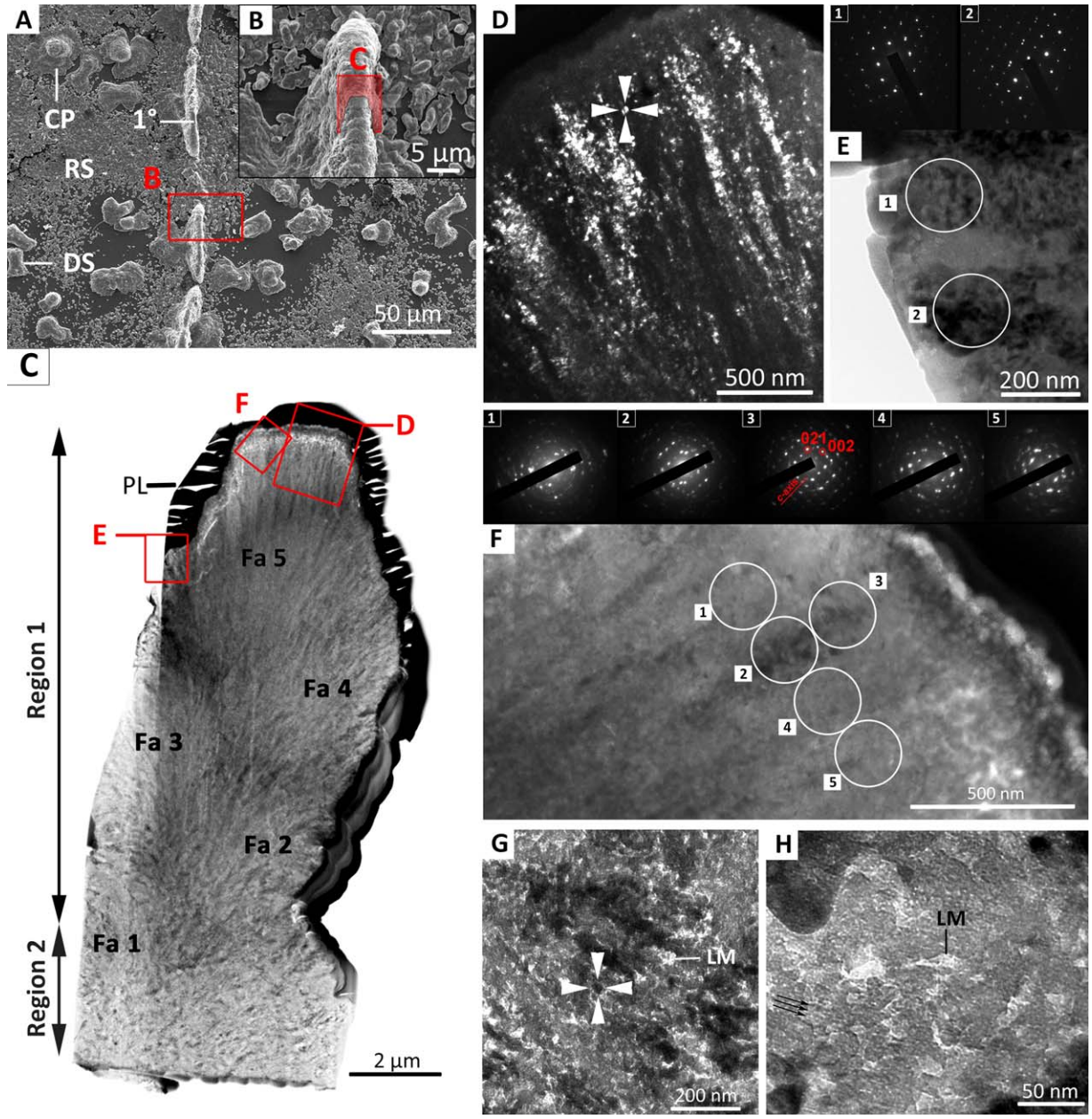

Fig. 3. *Pocillopora damicornis* primary septum in Stage C. (**A**) Top view of a primary septum (SEM). (**B**) Surface of the primary septum from which the FIB lamella was lifted out. (**C**) Overview of the FIB lamella in BF-TEM. (**D**) DF-TEM micrograph showing radiating bundles of fibers at the top of the primary septum (fasciculus 5). (**E**) Thinnest area of the FIB lamella showing bundles with distinctive single-crystal SAED patterns (1-2) (BF-TEM). (**F**) SAED patterns selected (200 nm in diameter) along almost uniform diffraction contrast of a bundle (selections 2-3) and in neighbors (1, 4, 5) at the top of the septum (BF-TEM). (**G**) Stacks of more or less structurally aligned submicrometer grains, 20–50 nm large (BF-TEM). Arrowheads point to individual submicrometer granular unit. (**H**) Typical lighter and beam-sensitive material in region 2 either surrounding granular units or organized as thin transverse striations (black arrows) (BF-TEM). CP: circular platelet; DS: dumbbell-like structure; Fa: fasciculus; RS: rod-shaped structures; LM: lighter and beam-sensitive material; PL: platinum layer; 1°: primary septum. [Color figure can be viewed in the online issue, which is available at wileyonlinelibrary.com.]

fusiform-like structures also occur during this stage (FC, Fig. 1B). The dumbbell-like and semispherulitic structures can also be observed *in vivo* using a binocular (Fig. 1B) and cannot therefore be artifacts of sample preparation. Within one and the same sample, one can recognize five different morphologies progressively evolving from dumbbell-like structures to semispherulites, as their length increases from 15 to 35 µm (Fig. 1F). All Raman spectra, acquired from different regions in several dumbbell-like and semispherulitic structures, indicate a purely aragonite mineralogy

(Gilis et al., 2014). Tilting of the sample during SEM observation reveal a flat underside facing the substrate, as illustrated in Figure 2A.

Dumbbell-like Structures

In the longitudinal FIB section lifted-out from the dumbbell-like deposit in Figure 2A, we centered the final thinning and cleaning at the transition area between the elongated (ER) and the fibro-radiating (RR) regions (Fig. 2A,B). In the thinned area two regions are distinguished in TEM (Fig. 2C,D). Region 1 contained bundles of fibers (Fig. 2D), slightly diverging toward the left and giving rise to the fibro-radiating external microstructure described above (RR, Fig. 2A). In region 2 (Fig. 2D,H), vertically oriented, loosely defined bundles were still recognized although fibrillar organization was not obvious. In this study, we consistently use the term "fiber" for the elongated structure composed of a single row of coherently aligned granular submicron structures 20–50 nm wide (Fig. 2E arrowheads) with a more translucent, beam-sensitive light material (LM, Fig. 2E) separating adjacent fibers. The term "bundle" is used to describe a set of 2 or more adjacent fibers with the same diffraction contrast (e.g., Fig. 2F, along selections 1–3). We never observed clean, acicular crystals.

The smallest aperture to record SAED patterns does not allow selection of specific regions of the sample smaller than 200 nm in diameter, preventing crystallographic analysis of individual fibers (20–50 nm wide). However, SAED patterns recorded in the small bundle of fibers displaying the strongest diffraction contrast in Fig. 2F (selections 1–3) are similar to those of aragonite single crystals viewed along the <110> plane, except for additional spots aligned along the $l = 2n$ rows of the reciprocal lattice. Moreover, continuous and spotty diffraction arcs, as opposed to sharp reflections, indicate small continuous and/or discontinuous misorientations of aragonite inside the selection. Selecting neighboring bundles (Fig. 2F, selections 4-5) yielded SAED patterns slightly modified compared to that of adjacent selection 3, indicating that adjoining bundles were crystallographically similar apart from a rotation around the *c*-axis. SAED patterns across strongly diverging fibers (Fig. 2G selections 1–4) also appeared practically identical but for a rotation of the *c*-axis closely mimicking the rotation of the fibers around their elongation.

The absence of perfect, single crystal diffraction patterns, even for the smallest selections along the bundle axis, might be partly ascribed to the stacking of several fibers in depth of the FIB sections, which were significantly thicker than the diameter of individual fibers (ca. 20–50 nm).

In the upper part of the dumbbell, (called "region 2" in Fig. 2D), some of these bundles looked like large clusters of coherently oriented 20–50 nm grains (Fig. 2H and inset). Again a beam-sensitive translucent, presumable light material appeared around grains or clusters (Fig. 2I).

Energy-dispersive X-ray spectroscopy (EDX) analysis yielded elemental composition of the FIB section, with an average Mg/Ca ratio of 7.04($\pm$0.70) mmol/mol and average Sr/Ca ratio of 7.98($\pm$0.40) mmol/mol.

Primary Septum

The FIB section removed from the primary septum (Fig. 3A,B) contained two structurally different regions (Fig. 3C). In the first major region, five different areas, 2–4 μm wide, could be distinguished according to difference in the global orientation of their aragonitic bundles and are described here as "fasciculi" (FA, Fig. 3C). Furthermore, TEM dark-field imaging exhibit the fibro-radiate microstructure as shown for the most apical fasciculus "Fa5" (Fig. 3D), with bundles of fibers lying normal to the external surface of the septum. Like in the dumbbells, the primary septum consists of 20–50 nm granular units (Fig. 3D, arrowheads), arranged in single-rows of similar diameter and forming a fiber, which are assembled into bundles. We did not observe any acicular crystals among these structures either, and fibers appeared less recognizable in the septa than in the dumbbell-like structures (Fig. 3D,F), which could be partly explained by a lower organization level in this ontogenetically young septum and/or by the larger thickness of this FIB section compared to that from the dumbbell.

A thinner area from the left side of the lamella allowed us to more easily distinguish a few larger bundles behaving like single-crystals, not fully crystallographically aligned with their neighbors (Fig. 3E, selections 1-2). Whether this observation of more regular bundles is related to the thickness of the section, or is a characteristic of the periphery of the septum during initiation of acicular crystal formation, could not be determined from our observations. Behind the fast-growing front of the septum (Fig. 3C, Fa 5) thin fibers appeared somewhat curved and subparallel to the FIB section (Fig. 3F). Despite this orientation, two SAED patterns selected (200 nm in diameter) along the almost uniform diffraction contrast of a bundle (Fig. 3F, selections 2-3) displayed quite clean < 1 0 0 > aragonite patterns indicating monocrystallinity with *c*-axis aligned along the axis of the bundle. Higher magnification imaging showed that bundles corresponded to stacks of more or less structurally aligned grains, 20–50 nm large (Fig. 3G). Finally, more randomly oriented grains, or grains arranged in stacks, made up the second and basal region of the FIB section (Fig. 3G,H). In both

regions 1 and 2, higher magnification revealed the presence of highly beam-sensitive light material around and inside granular structural units (Fig. 3G,H), producing lighter transverse striations (Fig. 3H).

Despite the loss of orientation with respect to septum morphology, crushed septa material displayed even clearer evidence of the features described above (Supporting Information Fig. S1).

Finally, elemental composition analyses of this FIB section with EDX, yielded a relatively higher Mg/Ca ratio in the septa of 11.06(±1.44) mmol/mol, while the Sr/Ca ratio was similar at 7.86(±0.41) mmol/mol, compared to the dumbbell.

DISCUSSION

While the occurrence, morphology, and spatial distribution of septa during skeletal ontogeny is the expression of a genetically coded body plan and require strong biological control (Clode et al., 2011; Cohen et al., 2009; Goreau and Hayes, 1977; Jell, 1980; Johnston, 1976; Le Tissier, 1988a,b; Vandermeulen and Watabe, 1973; Wainwright, 1963), randomly distributed dumbbell-like structures cannot be considered the result of the same highly controlled process(es). Dumbbell-like morphologies of calcium carbonate are easily produced without any active biological control through *in vitro* crystallization experiments in aqueous solution or in hydrated gel at high Mg/Ca ratio with *or without* organic additives (e.g., Cölfen and Qi, 2001; Falini et al., 2009, 2013; Fernandez-Diaz et al., 1996; Goffredo et al., 2011; Grassman et al., 2002; Jiao et al., 2006; Raz et al., 2000; Tang et al., 2009).

Conversely, because fusiform, dumbbell, and semispherulitic structures are observed *in vivo* (Fig. 1B), their occurrence cannot be ascribed to accidental precipitation induced by our sample preparation method (e.g., cleaning in sodium hypochlorite, rinsing with water, or dehydration in ethanol). Furthermore, we did not observe any of these structures on the substrate elsewhere than within the areas of the growing basal plates of recruits, where they might occur firmly fused with other $CaCO_3$ elements forming either the future columella or the basal plate. Hence, in our case, their formation cannot be explained by simple abiotic precipitation from seawater, but must be resulting from the conditions existing at the interface between the larval tissue and the substrate. Note that similar structures are in fact observable in previous studies of laterally growing skeleton on various flat substrates ("LSP" in Raz-Bahat et al., 2006: Fig. 1D; Tambutté et al., 2011; Venn et al., 2011, 2013).

The observed suite of dumbbell-spherulitic structures (Fig. 1F) conceivably is the result of a spherulitic growth sequence, starting from fusiform crystals, with radiating conic bundles subsequently developing at their tips, which finally reach a nearly spherical appearance. It is noted that such growth is comparable to the formation of category 2 spherulites in polymeric-based metal-carbonate *in vitro* crystallization assays with the following structural sequence: rod → dumbbell → twined sphere → sphere (e.g., Kniep and Busch, 1996; Busch et al., 1999; Yu and Cölfen, 2004; Gránásy et al., 2005; Xu and Yu, 2014).

Submicrometer Morphological Features

In septa and dumbbell-like structures alike, submicrometer grains appear either more or less structurally aligned into (pseudo) fibers, laterally assembled into bundles, or randomly stacked into larger clusters (the actual appearance might be a function of section orientation). Large acicular crystals were not observed in this study, but they are observed in mature septa-structures (Benzerara et al., 2011).

The dumbbell FIB section investigated here, although including only a quarter of the longitudinal organization of the dumbbell, allows us to confirm the fibro-radiating arrangement of crystals, which are fanning out from a central plane of fibrils lying almost parallel to the substrate (at the bottom of region 1, Fig. 2A–D).

In contrast, the primary septum is build by a superimposition of fasciculi composed of bundles of fibers with a fan-shaped microstructure. This organization suggests a different growth process than for dumbbell- and semispherulitic structures, which has no equivalent in purely abiotically formed minerals. Interestingly, fibers are systematically oriented quasi perpendicular to the external surface of the growing septum suggesting that material is deposited laterally for thickening and at the top for the elongation, for which the extension rate must be higher to give the shape of the septum (c.f. Brahmi et al., 2012b).

The relatively low degree of packing order and high porosity shown by TEM in both septum and dumbbell lamellae originate from their highly granular submicrometer fabric: 20–50 nm quasi-round units fill the bulk of these structures and also produce a characteristic granular external surface, observable in SEM (Gilis et al., 2014). This granularity, as opposed to homogenous and faceted crystals usually produced in purely inorganic precipitation, is often considered to be a signature of biologically induced or controlled Ca-carbonate mineralization in corals, and in many other biomaterials produced by invertebrate or bacteria (Isa, 1986; Stolarski, 2003; Cuif and Dauphin, 2005a,b; Stolarski and Mazur, 2005; Dauphin, 2006; Oaki et al., 2006; Rivadeneyra et al., 2006; Sethmann et al., 2006, 2007; Baronnet et al., 2008; Cusack et al., 2008; Przeniosło et al., 2008; Sánchez-Navas et al., 2009; Cuif et al., 2008,

2011; Goetz et al., 2011; Sondi et al., 2011; Weiner and Addadi, 2011; Schmahl et al., 2012a,b; 2013; Gilis et al., 2011, 2013; Péerez-Huerta et al., 2013). However, *in vitro* crystallization assays in a (hydro-)gel medium can produce similar calcium carbonate single-crystals composed of granular building blocks of less than 100 nm in diameter, often surrounded by a thin film of organic matrix (Grassmann et al., 2002; Cölfen Colfen and Antonietti, 2005; Imai et al., 2006; Oaki et al., 2006; for a review see Asenath-Smith et al., 2012; Falini et al., 2013; Sánchez-Navas et al., 2013).

Crystallographical Features

Fibers, at most 50 nm in diameter, observed here in both septa and dumbbells, are composed of one single row of granular units and already behave like single-crystals, a feature also observed in the skeleton of adult corals (Przeniosło et al., 2008; Benzerara et al., 2011; Motai et al., 2012; van de Locht et al., 2013) and in multiple other calcium carbonate biominerals (Oaki et al., 2006; Baronnet et al., 2008; Cuif et al., 2008; Cusack et al., 2008; Jacob et al., 2008; Politi et al., 2008; Przeniosło et al., 2008; Killian et al., 2009; Goetz et al., 2011; Weiner and Addadi, 2011; Nouet et al., 2012; Schmahl et al., 2012a,b; Zhang and Xu, 2013). All fibers belonging to either the dumbbell or primary septum have their elongation coincident with the aragonite *c*-axis, as also observed in adult coral (Benzerara et al., 2011). We additionally found that bundles up to 200 nm in diameter (corresponding to our smallest SAED selection), consisting of stacks of 2–10 parallel adjacent fibers packed into "cylindrical" structures, can share a common *c*-axis orientation while preserving rotational freedom of the *a*-*b* axes around it (Fig. 2F). In the granular regions of both septum and dumbbell, small and large aggregates of grains might also behave like single-crystal in some area while other aggregates are polycrystalline.

Classically, two main structural components are described in all adult coral skeleton septa, namely the Centers Of Calcification (COC) (Bourne, 1887; Ogilvie, 1897) [also referred to as 'Early Mineralization Zone' EMZ, *sensu* Cuif and Dauphin (2005a,b), or "Rapid Accretion Deposits" RAD *sensu* Stolarski (2003)] composed of large clusters of granular units that laterally grade into the fibrous skeleton, which is made of acicular crystals (or "Thickening Deposits," TD; *sensu* Stolarski, 2003). van de Locht et al. (2013) additionally observed, in a FIB foil extracted from adult coral skeleton, the presence of an intermediate region of partly aligned submicrometer grains into (pseudo)-fibers laterally assembled into stacks between the highly porous granular area (RAD) and dense acicular fibers (c.f. Fig. 3C,D in van de Locht et al., 2013). It was reasonably proposed that this represents the initiation of fiber growth starting with aggregation of submicrometer grains into granular bundles or cones and progressing to regular and elongated fibers. The (pseudo) fibers observed in the FIB lamella of the septum (Fig. 3C, region 2) correspond structurally to the intermediate region described by van de Locht et al. (2013). The absence of acicular fibers in the primary septa structure studied here suggests that in 2-days old recruits, these septa still consist only of the most rapidly growing components (i.e., RAD) plus this "intermediate" zone. It is very possible that acicular crystals would appear in the next growth stages of the septa, as suggested by the larger and more regular crystals shown in Fig. 3E and in a FIB foil obtained from the skeleton of a 5-days old recruit of *Acropora millepora* (van de Locht et al., 2013).

Chemical Composition

Higher average Mg/Ca molar ratios were measured in the septum section (~11 mmol/mol) compared with the dumbbell (~7 mmol/mol), whereas the Sr/Ca ratio remains comparable in both microstructures (around 8 mmol/mol).

In the adult skeleton of, *P. damicornis*, Brahmi et al. (2012a) measured Mg/Ca ratios varying between 2.2 mmol/mol in the slow growing areas, like in the ornamental spines, up to 13 mmol/mol in the fast growing RAD structures, suggesting a positive relationship between the local skeletal extension rate and the Mg/Ca ratio. Several other microanalytical studies have demonstrated substantial compositional heterogeneities of adult coral skeletons correlated with their ultrastructural components. For example, RADs are generally enriched in trace elements like Mg, Sr, S, Ba, and N, conceivably as a function of the amount and composition of organic materials embedded in these structures (Cuif et al., 2003; Sinclair et al., 2006; Gagnon et al., 2007; Meibom et al., 2004, 2006, 2007; Holcomb et al., 2009; Brahmi et al., 2010), and with relatively light stable isotope ratios such as $\delta^{13}C$, $\delta^{18}O$, and $\delta^{11}B$ (e.g., Adkins et al., 2003; Meibom et al., 2006; Blamart et al., 2007; Rollion-Bard et al., 2010) compared to adjacent TD.

Different hypotheses have been proposed to explain nonclassical crystallization pathways in carbonate biomineralization, including amorphous calcium carbonate (ACC) (Addadi et al., 2003; Politi et al., 2008; Pouget et al., 2009; Weiner et al., 2009; Weiner and Addadi, 2011; Gong et al., 2012; Zhang and Xu, 2013), self-assembly of mesocrystals (Colfen and Mann, 2003; Colfen and Antonietti, 2005; Song and Colfen, 2010), and self-organization/bridged-crystals (Imai et al., 2006; Oaki et al., 2006; Przeniosło et al., 2008). Some of these implicitly involve a gel-like matrix or media,

from which the carbonate structures in question precipitate.

Based on the morphology, distribution, ultrastructure, and chemistry of the dumbbell- to spherulitic structures, which are transiently present on the basal plate of 2-days old recruits of *Pocillopora damicornis* settled on a flat substrate, we suggest that they might result from a less controlled precipitation in the gel-like environment, which is likely to exist at the interface between the substrate and the coral tissue during settlement. In contrast, primary skeletal structures, such as septa, form under strong and genetically dictated biological control. Our observations highlight the inherent difficulties involved in distinguishing different biomineralization pathways based on ultrastructural and crystallographical observations. Submicrometer granular textures, which are so commonly observed in biocarbonates, might provide little, if any, specific information about the process through which a biocarbonate is formed.

ACKNOWLEDGMENTS

The authors owe special thanks to Michel Hignette, Dominique Duché, Jean-Daniel Galois, Sylvain Joumier, Nicolas Luys, Thierry Carré, Fabrice Cesari-Colonna, Laurent Petit, Deodat Manchon at the Aquarium Tropical, Palais de la Porte Dorée in Paris, for their assistance with coral manipulation and aquarium maintenance. The authors thank Claude Henry and Cecile Hebert for access to their microscopy facilities, at the Centre Interdisciplinaire de Nanosciences de Marseille (CINaM) and Interdisciplinary Centre for Electron Microscopy (EPFL, Lausanne), respectively. The authors owe thanks to Dr. Aicha Hessler, Dr. Marco Cantoni, and Pr. Philippe Buffat and for assistance in EDX acquisition and data analyses, and to Martiane Cabie (CP2M, Marseille) and Fabienne Bobard for FIB lamella preparation.

LITERATURE CITED

Addadi L, Raz S, Weiner S. 2003. Taking advantage of disorder: Amorphous calcium carbonate and its roles in biomineralization. Adv Mater 15:959–970.

Adkins JF, Boyle EA, Curry WB, Lutringer A. 2003. Stable isotopes in deep-sea corals and a new mechanism for "vital effects". Geochim Cosmochim Acta 667:1129–1143.

Asenath-Smith E, Li H, Keene EC, Seh ZW, Estroff LA. 2012. Crystal growth of calcium carbonate in hydrogels as a model of biomineralization. Adv Funct Mater 22:2891–2914.

Barnes DJ. 1970. Coral skeletons: An explanation of their growth and structure. Science 170:1305–1308.

Baronnet A, Cuif JP, Dauphin Y, Farre B, Nouet J. 2008. Crystallization of biogenic Ca-carbonate within organo-mineral micro-domains. Structure of the calcite prisms of the pelecypod pinctada margaritifera (mollusca) at the submicron to nanometre ranges. Mineral Mag 72:539–548.

Benzerara K, Menguy N, Obst M, Stolarski J, Mazur M, Tylisczak T, Brown GE, Meibom A. 2011. Study of the crystallographic architecture of corals at the nanoscale by scanning transmission X-ray microscopy and transmission electron microscopy. Ultramicroscopy 111:1268–1275.

Blamart D, Rollion-Bard C, Meibom A, Cuif JP, Juillet-Leclerc A, Dauphin Y. 2007. Correlation of boron isotopic composition with ultrastructure in the deep-sea coral lophelia pertusa: Implications for biomineralization and paleo-pH. Geochem Geophy Geosy 8:Q12001.

Bourne GC. 1887. Memoirs: On the anatomy of mussa and euphyllia, and the morphology of the madreporarian skeleton. Q J Microsc Sci 2:21–51.

Brahmi C, Kopp C, Domart-Coulon I, Stolarski J, Meibom A. 2012a. Skeletal growth dynamics linked to trace-element composition in the scleractinian coral pocillopora damicornis. Geochim Cosmochim Acta 99:146–158.

Brahmi C, Domart-Coulon I, Rougee L, Pyle DG, Stolarski J, Mahoney JJ, Richmond RH, Ostrander GK, Meibom A. 2012b. Pulsed Sr-86-labeling and NanoSIMS imaging to study coral biomineralization at ultra-structural length scales. Coral Reefs 31:741–752.

Brahmi C, Meibom A, Smith DC, Stolarski J, Auzoux-Bordenave S, Nouet J, Doumenc D, Djediat C, Domart-Coulon I. 2010. Skeletal growth, ultrastructure and composition of the azooxanthellate scleractinian coral balanophyllia regia. Coral Reefs 29:175–189.

Bryan WH, Hill D. 1941. Spherulitic crystallization as a mechanism of skeletal growth in the hexacorals. Proc R Soc Queensl 52:78–91.

Busch S, Dolhaine H, DuChesne A, Heinz S, Hochrein O, Laeri F, Podebrad O, Vietze U, Weiland T, Kniep R. 1999. Biomimetic morphogenesis of Fluorapatite-gelatin Composites- fractal growth, the question of intrinsic electric fields, core: Shell assemblies, hollow spheres and reorganization of denatured collagen. Eur J Inorg Chem 1643–1653.

Clode PL, Lema K, Saunders M, Weiner S. 2011. Skeletal mineralogy of newly settling acropora millepora (scleractinia) coral recruits. Coral Reefs 30:1–8.

Clode PL, Marshall AT. 2002a. Low temperature FESEM of the calcifying interface of a scleractinian coral. Tissue Cell 34: 187–198.

Clode PL, Marshall AT. 2002b. Low temperature X-ray microanalysis of calcium in a scleractinian coral: Evidence of active transport mechanisms. J Exp Biol 205:3543–3552.

Clode PL, Marshall AT. 2003. Calcium associated with a fibrillar organic matrix in the scleractinian coral galaxea fascicularis. Protoplasma 220:153–161.

Cohen AL, McCorkle DC, de Putron S, Gaetani GA, Rose KA. 2009. Morphological and compositional changes in the skeletons of new coral recruits reared in acidified seawater: Insights into the biomineralization response to ocean acidification. Geochem Geophy Geosys 10:1–12

Colfen H, Antonietti M. 2005. Mesocrystals: Inorganic superstructures made by highly parallel crystallization and controlled alignment. Angew Chem Int Ed Engl 44:5576–5591.

Colfen H, Mann S. 2003. Higher-order organization by mesoscale self-assembly and transformation of hybrid nanostructures. Angew Chem Int Ed Engl 42:2350–2365.

Cölfen H, Qi L. 2001. A systematic examination of the morphogenesis of calcium carbonate in the presence of a Double-hydrophilic block copolymer. Chem Eur J 7:106–116.

Constantz BR. 1986. Coral skeleton construction: A physiological dominated process. Palaios 1:152–157.

Cuif J, Dauphin Y, Doucet J, Salomé M, Susini J. 2003. XANES mapping of organic sulfate in three scleractinian coral skeletons. Geochim Cosmochim Acta 67:75–83.

Cuif JP, Dauphin Y. 2005a. The environment recording unit in coral skeletons – a synthesis of structural and chemical evidences for a biochemically driven, stepping-growth process in fibres. Biogeosciences 2:61–73.

Cuif JP, Dauphin Y. 2005b. The two-step mode of growth in the scleractinian coral skeletons from the micrometre to the overall scale. J Struct Biol 150:319–331.

Cuif J-P, Dauphin Y, Sorauf JE, 2011. Biominerals and Fossils Through Time, Cambridge, UK, Cambridge University Press.

Cuif JP, Dauphin Y, Farre B, Nehrke G, Nouet J, Salome M. 2008. Distribution of sulphated polysaccharides within calcareous biominerals suggests a widely shared two-step crystallization process for the microstructural growth units. Mineral Mag 72:233–237.

Cusack M, Dauphin Y, Cuif J, Salome M, Freer A, Yin H. 2008. Micro-XANES mapping of sulphur and its association with magnesium and phosphorus in the shell of the brachiopod, terebratulina retusa. Chem Geol 253:172–179.

Dauphin Y. 2006. Mineralizing matrices in the skeletal axes of two corallium species (alcyonacea). Comp Biochem Physiol Part A. 145:54–64.

Falini G, Fermani S, Tosi G, Dinelli E. 2009. Calcium carbonate morphology and structure in the presence of seawater ions and humic acids. Cryst Growth Des 9:2065–2072.

Falini G, Reggi M, Fermani S, Sparla F, Goffredo S, Dubinsky Z, Levi O, Dauphin Y, Cuif JP. 2013. Control of aragonite deposition in colonial corals by intra-skeletal macromolecules. J Struct Biol 183:226–238.

Fernández Díaz L, Putnis A, Prieto M, Putnis CV. 1996. The role of magnesium in the crystallization of calcite and in a porous medium. J Sediment Res 66:482–491.

Gagnon AC, Adkins J, Fernandez D, Robinson L. 2007. Sr/ca and mg/ca vital effects correlated with skeletal architecture in a scleractinian deep-sea coral and the role of rayleigh fractionation. Earth Planet Sci Lett 261:280–295.

Gilis M, Grauby O, Willenz P, Dubois P, Heresanu V, Baronnet A. 2013. Biomineralization in living hypercalcified demosponges: Toward a shared mechanism? J Struct Biol 183: 441–454.

Gilis M, Grauby O, Willenz P, Dubois P, Legras L, Heresanu V, Baronnet A. 2011. Multi-scale mineralogical characterization of the hypercalcified sponge petrobiona massiliana (calcarea, calcaronea). J Struct Biol 176:315–329.

Gilis M, Meibom A, Domart-Coulon I, Grauby O, Stolarski J, Baronnet A. 2014. Biomineralization in newly settled recruits of the scleractinian coral pocillopora damicornis. J Morphol 272:1349–1365. Doi: 10.1002/jmor.20307

Gladfelter EH. 1982. Skeletal development in acropora cervicornis- I. Patterns of calcium carbonate accretion in the axial corallite. Coral Reefs 1:45–51.

Gladfelter EH. 1983. Skeletal development in acropora cervicornis II. Diel patterns of calcium carbonate accretion. Coral Reefs 2:91–100.

Goetz AJ, Steinmetz DR, Griesshaber E, Zaefferer S, Raabe D, Kelm K, Irsen S, Sehrbrock A, Schmahl WW. 2011. Interdigitating biocalcite dendrites form a 3-D jigsaw structure in brachiopod shells. Acta Biomater 7:2237–2243.

Goffredo S, Vergni P, Reggi M, Caroselli E, Sparla F, Levy O, Dubinsky Z, Falini G. 2011. The skeletal organic matrix from mediterranean coral balanophyllia europaea influences calcium carbonate precipitation. PLoS One 6:e22338-

Gong YUT, Killian C, Olson IC, Appathurai NP, Amasino AL, Martin MC, Holt LJ, Wilt FH, Gilbert PUPA. 2012. Phase transitions in biogenic amorphous calcium carbonate. Proc Natl Acad Sci USA 109:6088–6093.

Goreau, N.I, Hayes, R.L, 1977. Nucleation catalysis in coral skeletogenesis. D.L. in Taylor (ed.) Proceedings of Third International Coral Reef Symposium Vol. 2: Geology. Rosenstiel School of Marine and Atmospheric Science, Miami, Florida. 2, 439–445.

Gránásy L, Pusztai T, Tegze G, Warren JA, Douglas JF, 2005. Growth and form of spherulites. Phys Rev E 72:1–15.

Grassman O, Müller G, Löbmann P. 2002. Organic-inorganic hybrid structure of calcite crystalline assemblies grown in a gelatin hydrogel Matrix- relevance to biomineralization. Chem Mater 14:4530–4535.

Holcomb M, Cohen AL, Gabitov RI, Hutter JL. 2009. Compositional and morphological features of aragonite precipitated experimentally from seawater and biogenically by corals. Geochim Cosmochim Acta 73:4166–4179.

Houlbrèque F, Meibom A, Cuif JP, Stolarski J, Marrocchi Y, Ferrier-Pagès C,Domart-Coulon I, Dunbar RB. 2009. Strontium-86 labeling experiments show spatially heterogeneous skeletal formation in the scleractinian coral porites porites. Geophys Res Lett 36:1–16.

Imai H, Oaki Y, Kotachi A. 2006. A biomimetic approach for hierarchically structured inorganic crystals through Self-organization. Bull Chem Soc Japan 79:1834–1851.

Isa Y. 1986. An electron microscope study on the mineralization of the skeleton of the staghorn coral acropora hebes. Mar Biol 93:91–101.

Jacob D, Soldati A, Wirth R, Huth J, Wehrmeister U, Hofmeister W. 2008. Nanostructure, composition and mechanisms of bivalve shell growth. Geochim Cosmochim Acta 72: 5401–5415.

Jell JS. 1974. The microstructure of some scleractinian corals. In Cameron AM editor Proceedings of Second International Coral Reef Symposium, Great Barrier Reef Committee, Brisbane, Australia. pp. 301–320

Jell JS. 1980. Skeletogenesis of newly settled planulae of the hermatypic coral porites lutea. Acta Palaeontol Pol 25:311–320.

Jiao Y, Feng Q, Li X. 2006. The co-effect of collagen and magnesium ions on calcium carbonate biomineralization. Mater Sci Eng C. 26:648–652.

Johnston IS. 1976. The tissue-skeleton interface in newly settled polyps of the reef coral *Pocillopora damicornis*. In: Watanabe N, Wilbur KM editors. The Mechanisms of Mineralization in Invertebrates and Plants, Symp Georgetown, S.C., U. of S.C. Press, Columbia.

Johnston, I.S, 1978. Functional ultrastructure of the skeleton and the skeletogenic tissues of the reef coral Pocillopora damicornis. PhD Dissertation, Univ Calif LA.

Johnston IS. 1980. The ultrastructure of skeletogenesis in hermatypic corals. Int Rev Cytol 67:171–214.

Juillet-Leclerc A, Reynaud S, Rollion-Bard C, Cuif JP, Dauphin Y, Blamart D, Ferrier-Pages C, Allemand D. 2009. Oxygen isotopic signature of the skeletal microstructures in cultured corals: Identification of vital effects. Geochim Cosmochim Acta 73:5320–5332.

Killian CE, Metzler RA, Gong YUT, Olson IC, Aizenberg J, Politi Y, Wilt FH, Scholl A, Young A, Doran A, Kunz M, Tamura N, Coppersmith SN, Gilbert PUPA. 2009. Mechanism of calcite co-orientation in the sea urchin tooth. J Am Chem Soc 131:18404–18409.

Kniep R, Busch S. 1996. Biomimetic growth and Self-assembly of fluorapatite aggregates by diffusion into denatured collagen matrices. Angew Chem Int Ed 35:2624–2626.

Le Tissier MDAA. 1988a. Patterns of formation and the ultrastructure of the larval skeleton of pocillopora damicornis. Mar Biol 98:493–501.

Le Tissier MDAA. 1988b. Diurnal patterns of skeleton formation in pocillopora damicornis (linnaeus). Coral Reefs 7: 81–88.

Le Tissier MDAA. 1991. The nature of the skeleton and skeletogenic tissues in the cnidaria. Hydrobiologia 216/217:397–402.

Lowenstam, H.A, Weiner, S, 1989. On Biomineralization, New York: Oxford University Press.

Mann, S, 2001. Biomineralization: Principles and Concepts in Bioinorganic Materials Chemistry, Oxford University Press.

Meibom A, Cuif JP, Hillion F, Constantz BR, Juillet-Leclerc A, Dauphin Y, Watanabe T, Dunbar RB. 2004. Distribution of magnesium in coral skeleton. Geophys Res Lett 31:L23306. Doi:23310.21029/22004GL021313.

Meibom A, Cuif JP, Houlbreque F, Mostefaoui S, Dauphin Y, Meibom KL, Dunbar RB. 2008. Compositional variations at ultra-structure length scales in coral skeleton. Geochim Cosmochim Acta 72:1555–1569.

Meibom A, Mostefaoui S, Cuif JP, Dauphin Y, Houlbreque F, Dunbar RB, Constantz B. 2007. Biological forcing controls the chemistry of reef-building coral skeleton. Geophys Res Lett 34:L02601. DOI: 10.1029/2006GL028657.

Meibom A, Yurimoto H, Cuif JP, Domart-Coulon I, Houlbreque F, Constantz B, Dauphin Y, Tambutte E, Tambutte S, Allemand D, Wooden J. 2006. Vital effects in coral skeletal composition display strict three-dimensional control. Geophys Res Lett 33:L11608. Doi:11610.11029/12006GL025968.

Motai S, Nagai T, Sowa K, Watanabe T, Sakamoto N, Yurimoto H, Kawano J. 2012. Needle-like grains across growth lines in the coral skeleton of porites lobata. J Struct Biol 180:389–393.

Nouet J, Baronnet A, Howard L. 2012. Crystallization in organo-mineral micro-domains in the crossed-lamellar layer of nerita undata (gastropoda, neritopsina). Micron 43:456–462.

Oaki Y, Kotachi A, Miura T, Imai H. 2006. Bridged nanocrystals in biominerals and their biomimetics: Classical yet modern crystal growth on the nanoscale. Adv Funct Mater 16: 1633–1639.

Ogilvie M. 1897. Microscopic and systematic study of madreporarian types of corals. Phil Trans R Soc B 187:83–345.

Perez-Huerta A, Dauphin Y, Cusack M. 2013. Biogenic calcite granules–are brachiopods different?. Micron 44:395–403.

Politi Y, Metzler RA, Abrecht M, Gilbert B, Wilt FH, Sagi I, Addadi L, Weiner S, Gilbert PUPA. 2008. Transformation mechanism of amorphous calcium carbonate into calcite in the sea urchin larval spicule. Proc Natl Acad Sci USA 105: 17362–17366.

Pouget EM, Bomans PH, Goos JA, Frederik PM, de With G, Sommerdijk NAJM. 2009. The initial stages of template-controlled CaCO3 formation revealed by cryo-TEM. Science 323:1455–1458.

Przeniosło R, Stolarski J, Mazur M, Brunelli M. 2008. Hierarchically structured scleractinian coral biocrystals. J Struct Biol 161:74–82.

Raz S, Weiner S, Addadi L. 2000. Formation of high-magnesian calcites via an amorphous precursor phase: Possible biological implications. Adv Mater 12:38–42.

Raz-Bahat M, Erez J, Rinkevich B. 2006. In vivo light-microscopic documentation for primary calcification processes in the hermatypic coral stylophora pistillata. Cell Tissue Res 325:361–368.

Ries JB, Stanley SM, Hardie LA. 2006. Scleractinian corals produce calcite, and grow more slowly, in artificial cretaceous seawater. Geology 34:525-

Rivadeneyra MA, Martín-Algarra A, Sánchez-Navas A, Martíin-Ramos D. 2006. Carbonate and phosphate precipitation by chromohalobacter marismortui. Geomicrobiol J 23:89–101.

Robinson LF, Adkins JF, Frank N, Gagnon AC, Prouty NG, et al,. 2014. The geochemistry of deep-sea coral skeletons: A review of vital effects and applications for palaeoceanography. Deep-Sea Res II 99:184–198.

Rollion-Bard C, Blamart D, Cuif JP, Dauphin Y. 2010. In situ measurements of oxygen isotopic composition in deep-sea coral, lophelia pertusa: Re-examination of the current geochemical models of biomineralization. Geochim Cosmochim Acta 74:1338–1349.

Sánchez-Navas A, Martín-Algarra A, Sánchez-Román M, Jiménez-López C, Nieto F, et al,. 2009. Crystal-growth behavior in Ca-mg carbonate bacterial spherulites. Cryst Growth Des 9:2690–2699.

Sánchez-Navas A, Martín-Algarra A, Sánchez-Román MN, Jiménez-López CN, Nieto F, Ruiz-Bustos A. 2013. Crystal Growth of Inorganic and Biomediated Carbonates and Phosphates. In: Sukarno Olavo F, editor. Advanced Topics on Crystal Growth, InTech, Rijeka, Croatia.

Schmahl WW, Griesshaber E, Kelm K, Ball A, Goetz A, et al,. 2012b. Towards systematics of calcite biocrystals: Insight from the inside. Z Kristallogr Cryst Mater 227:604–611.

Schmahl WW, Griesshaber E, Kelm K, Goetz A, Jordan G, et al,. 2012a. Hierarchical structure of marine shell biomaterials: Biomechanical functionalization of calcite by brachiopods. Z Kristallogr - Cryst Mater 227:793–804.

Sethmann I, Helbig U, Wörheide G. 2007. Octocoral sclerite ultrastructures and experimental approach to underlying biomineralization principles. Cryst Eng Comm 9:1262–1268.

Sethmann I, Hinrichs R, Wörheide G, Putnis A. 2006. Nanocluster composite structure of calcitic sponge spicules—a case study of basic characteristics of biominerals. J Inorg Biochem 100:88–96.

Sinclair DJ, Williams B, Risk M. 2006. A biological origin for climate signals in corals—trace element "vital effects" are ubiquitous in scleractinian coral skeletons. Geophys Res Lett 33:L17707.

Sondi I, Salopek-Sondi B, Skapin SD, Segota S, Jurina I, Vukelic B. 2011. Colloid-chemical processes in the growth and design of the bio-inorganic aragonite structure in the scleractinian coral cladocora caespitosa. J Colloid Interface Sci 354: 181–189.

Song RQ, Colfen H. 2010. Mesocrystals–ordered nanoparticle superstructures. Adv Mater 22:1301–1330.

Stolarski J. 2003. Three−dimensional micro− and nanostructural characteristics of the scleractinian coral skeleton: A biocalcification proxy. Acta Palaeontol Pol. 48:497–530.

Stolarski J, Mazur M. 2005. Nanostructure of biogenic versus abiogenic calcium carbonate crystals. Acta Palaeontol Pol. 50: 847–865.

Tambutté E, Allemand D, Zoccola D, Meibom A, Lotto S, Caminiti N, Tambutte S. 2007. Observations of the tissue-skeleton interface in the scleractinian coral stylophora pistillata. Coral Reefs 26:517–529.

Tambutté E, Tambutté S, Segonds N, Zoccola D, Venn A, Erez J, Allemand D. 2011. Calcein labelling and electrophysiology: Insights on coral tissue permeability and calcification. Proc R Soc Biol Sci Ser B 279:19–27. doi: 10.1098/rspb.2011.0733.

Tang H, Yu J, Zhao X. 2009. Controlled synthesis of crystalline calcium carbonate aggregates with unusual morphologies involving the phase transformation from amorphous calcium carbonate. Mater Res Bull 44:831–835.

van de Locht R, Verch A, Saunders M, Dissard D, Rixen T, Moya A, Kroger R. 2013. Microstructural evolution and nanoscale crystallography in scleractinian coral spherulites. J Struct Biol 183:57–65.

Vandermeulen JH, Watabe N. 1973. Studies on reef corals. I. Skeleton formation by newly settled planula larva of pocillopora damicornis. Mar Biol 23:47–57.

Veis A. 2005. Materials science. A window on biomineralization. Science 307:1419–1420.

Venn A, Tambutte E, Holcomb M, Allemand D, Tambutte S. 2011. Live tissue imaging shows reef corals elevate pH under their calcifying tissue relative to seawater. PLoS One 6: e20013

Venn A, Tambutté E, Holcomb M, Laurent J, Allemand D, Tambutté S. 2013. Impact of seawater acidification on pH at the tissue–skeleton interface and calcification in reef corals. Proc Natl Acad Sci USA 110:1634–1639.

Wainwright SA. 1963. Skeletal organization in the coral, pocillopora damicornis. Q J Microsc Sci 104:169–183.

Weber JN. 1973. Incorporation of strontium into reef coral skeletal carbonate. Geochim Cosmochim Acta 37:2173–2190.

Weiner S, Addadi L. 2011. Crystallization pathways in biomineralization. Annu Rev Mater Res 41:21–40.

Weiner S, Mahamid J, Politi Y, Ma Y, Addadi L. 2009. Overview of the amorphous precursor phase strategy in biomineralization. Front Mater Sci China 3:104–108.

Xu S, Yu P. 2014. A rapid, green and versatile route to synthesize metal carbonate superstructures via the combination of regenerated silk fibroin and compressed co2. Cryst Eng Comm 16:1311

Yu SH, Cölfen H. 2004. Bio-inspired crystal morphogenesis by hydrophilic polymers. J Mat Chem 14:1311–1321.

Zhang G, Xu J. 2013. From colloidal nanoparticles to a single crystal: New insights into the formation of nacre's aragonite tablets. J Struct Biol 182:36–43.